ISSN (Print) 1226-1750
ISSN (Online) 2233-6656
Journal of Magnetics 25(4), 524-533 (2020) https://doi.org/10.4283/JMAG.2020.25.4.524

7 Tesla Magnetic Resonance Image Radio-Frequency Coils for Measuring Lithium-Ion Battery Cell Performance

Dan Bi Song[1] and Yeunchul Ryu[2]*

[1]*Department of Health Sciences and Technology, GAIHST, Gachon University, Incheon 21999, Republic of Korea*
[2]*Department of Radiological Science, Gachon University, Incheon 13120, Republic of Korea*

(Received 12 November 2020, Received in final form 16 December 2020, Accepted 16 December 2020)

In recent years, studies have been conducted to confirm the battery charge/discharge state using a magnetic resonance (MR) system. However, due to the structural characteristics of the battery, some difficulties exist in acquiring the signal. For example, because a loop coil does not coincide with the battery cell structure, non-uniform areas exist inside the cell samples, and it works as a limit to acquiring a quantitative MR signal measuring from the pack of lithium-ion batteries (LIB). In addition, the radio-frequency (RF) signals are weakened by the aluminum layer of the cell package. In this paper, we proposed a planar RF coil to obtain uniform ^{1}H and ^{7}Li signals from this shielding-packaged battery cell in 7 Tesla (T) magnetic resonance image (MRI). To demonstrate the usefulness of the proposed planar RF coil, we designed a loop coil for ^{1}H and ^{7}Li, a planar coil for ^{1}H, and a cut coil for ^{1}H and ^{7}Li. Then the performance of each coil was compared through a bench test. The water phantom image was acquired with each coil, and the signal intensity profile and signal-to-noise ratio (SNR) were calculated and compared. The ^{1}H/^{7}Li images and spectra of the electrolyte phantom were obtained using the cut coils, and the results were compared with the phantom.

Keywords : lithium-ion battery, radio-frequency coil, 7 Tesla, magnetic resonance image

1. Introduction

A battery converts the chemical energy of active material into electrical energy through an electrochemical oxidation-reduction reaction. Batteries are typically assemblies of two or more cells in, but sometimes include single cells. As a battery is used, the battery voltage gradually decreases and eventually reaches a state in which the battery cannot operate any device. In this case, a battery that cannot be used again is disposable. A representative example is the dry battery widely used in everyday life. In contrast, a battery that can be recharged and reused after being discharged is a reusable or storage battery. Reusable batteries are widely applied to wireless electronic products such as laptops and cell phones [1, 2]. Lithium-ion batteries are reusable batteries and have been widely used in mobile electronic devices, including cell phones and laptops, for about 20 years, and their usage is now expanding to the field of electric vehicles [3]. The charging/discharging mechanism of lithium-ion batteries is illustrated in Fig. 1. The mechanism of charging is presented in Fig. 1(a). The first battery charge is conducted in the manufacturing process, and lithium ions are transferred from the lithium compound in the anode to the cathode. Simultaneously, electrons move from the anode to the cathode through the conducting wire. The mechanism of discharge goes through the opposite process. As presented in Fig. 1(b), lithium ions leave the cathode and move to the anode, and electrons return to the anode through the conducting wire.

Along with the development of battery technology, efforts continue to ensure safety during charging and discharging. As part of the efforts, studies have recently assessed the battery charging/discharging state using a magnetic resonance (MR) system [4-7]. Such studies enable the observation of phenomena occurring inside the batteries, such as the formation of dendritic crystals on the electrode surface and electrical/chemical changes in the charging/discharging states, and help discover defects that can hardly be identified with the naked eye [8-11].

However, when considering the flat structure of batteries, determining the shape of the RF coils that can be optimized for the battery structure is more important than

*Corresponding author: Tel: +82-32-820-4410
Fax: +82-32-822-8251, e-mail: yeunchul.ryu@gachon.ac.kr

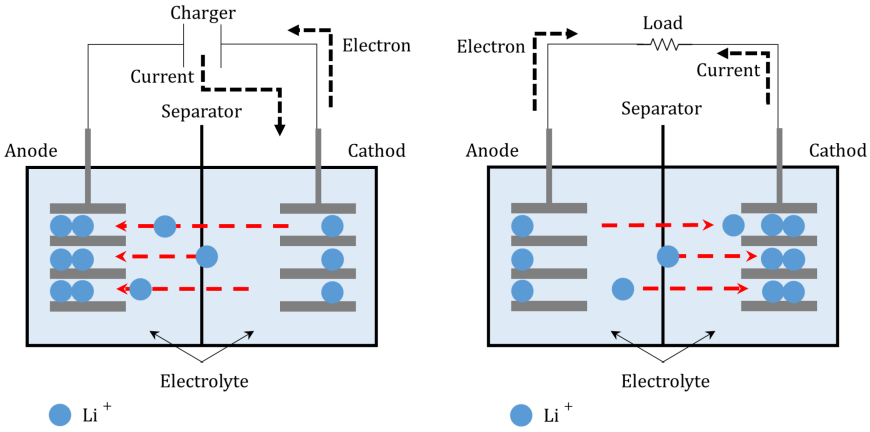

Fig. 1. (Color online) Illustration of the basic charging/discharging process of LIB (a) charging operation of LIB cell and (b) discharging operation of LIB cell.

anything else. For example, because the loop RF coils do not match the battery cell structure, non-uniform regions of the magnetic field occur inside battery cells; thus, limitations exist in obtaining MR signals. In addition, the aluminum substrate in batteries blocks RF signals, consequently weakening MR signals.

In this study, a planar RF coil is proposed to obtain uniform ^{1}H and ^{7}Li signals from battery cells in a 7T MRI system to overcome such problems. To prove the usefulness of the proposed planar, loop and planar coils are designed, and the performance of the individual coils are compared through a bench test. Water phantom images are acquired with individual coils to investigate the effects of the coil shapes on the phantom. Thereafter, the signal-to-noise ratios (SNRs) of the individual images are measured, and the results are compared. In addition, the ^{1}H and ^{7}Li images and spectra of the electrolyte phantom are obtained with the proposed planar coils for ^{1}H and ^{7}Li, and the results for diverse phantoms are compared.

2. Materials and Methods

2.1. Design of Loop Radio-Frequency Coils for ^{1}H and ^{7}Li

Loop coils for ^{1}H and ^{7}Li that can be operated in 7T MRI were fabricated. The loop coil for ^{1}H in Fig. 2 is a circular coil with an inner diameter of 20 mm and was tuned to 297.2 MHz, which is the resonance frequency of ^{1}H at 7T, using three 22-pF capacitors and variable capacitors. In addition, to minimize the reflection caused by the difference in impedance between the connection ends of the coil and the MR system, the impedance of the coil connection end was matched to 50 Ω as with the connection end of the MR system using a variable capacitor. The loop coil for ^{7}Li in Fig. 3 is a circular coil with an inner diameter of 20 mm, and was tuned to 115

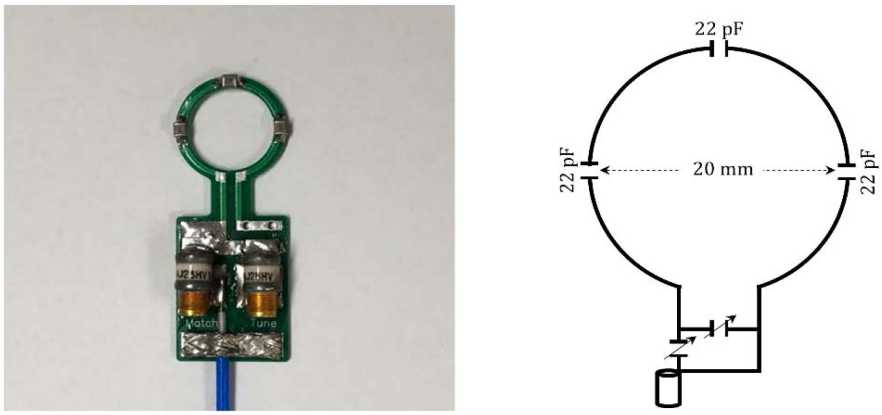

Fig. 2. (Color online) Loop coil for ^{1}H (a) image of implemented ^{1}H loop coil and (b) diagram of implemented ^{1}H loop coil.

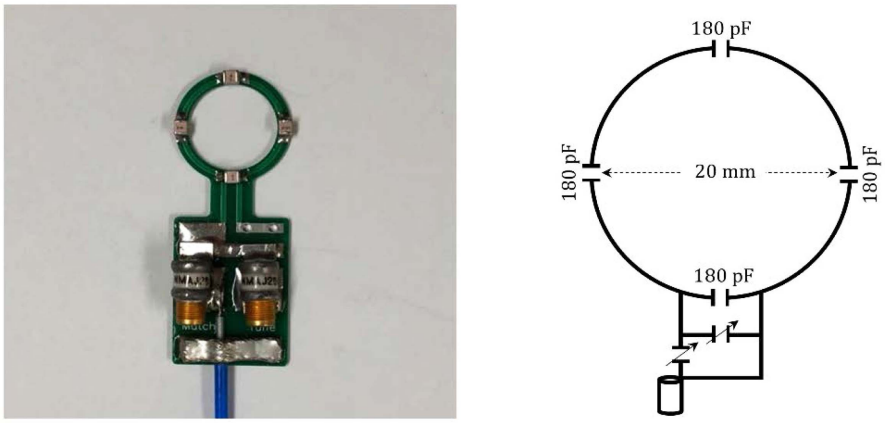

Fig. 3. (Color online) Loop coil for ^{7}Li (a) image of implemented ^{7}Li loop coil and (b) diagram of implemented ^{7}Li loop coil.

MHz, which is the resonance frequency of ^{7}Li at 7T, using four 180-pF capacitors and variable capacitors, and matched to 50 Ω. The reflection coefficient (S_{11}) was measured with a network analyzer (Keysight N9913A, Keysight Technologies, Santa Rosa, CA, USA) to identify the tuning and matching of the manufactured coils. The efficiency of the coil was calculated through the reflection coefficient. The index representing this is called a quality factor (Q-factor). A larger Q-factor value leads to the better selectivity for the resonant coil frequency. Thus, the bandwidth becomes narrow and sharp.

2.2. First Design of Planar Radio-Frequency Coil for ^{1}H

Battery cells are small and flat and have small samples that can be visualized. Given these characteristics, the following coil conditions can be optimized for the battery cell structure. First, coils must be rectangular and fit the shape of the battery cells. Second, the sensitivity of the coils must be maximized. This condition can be met by designing a small coil that minimizes the volume and makes the gap between the coil and the battery cell as close as possible. Third, uniform B_1 field must be formed over all areas of the battery cell. One of the obstacles to having a uniform B_1 field distribution is the "fringe effect." The fringe effect refers to the amorphous electric force lines distributed between conductors through which high-frequency alternating currents flow. In particular, the fringe effect occurs strongly in long and flat strips, and the primary cause of the fringe effect is the eddy current generated when the magnetic field changes according to Faraday's law [12]. In this case, the fringe effect can be reduced by minimizing the current concentration at the conductor edge by making the distance of the conductor strip small and reducing the magnetic flux of the outer range.

A planar coil to satisfy the above condition is illustrated in Fig. 4. A gap of 3 mm was placed between the two acrylic plates of size 110 mm × 25 mm so that the battery cells could be located as close as possible between them. The two acrylic plates were then wrapped with a 25-mm-wide conductor strip to form a "U" shape. The size of the conductor in each acrylic plate was 40 mm × 25 mm. Because the conductor strips were very close to each other, currents of almost the same size in opposite directions flowed through the conductor strips of individual acrylic plates in this structure. This situation can minimize the fringe effect because the magnetic flux in the outer region of the coil becomes almost zero [13].

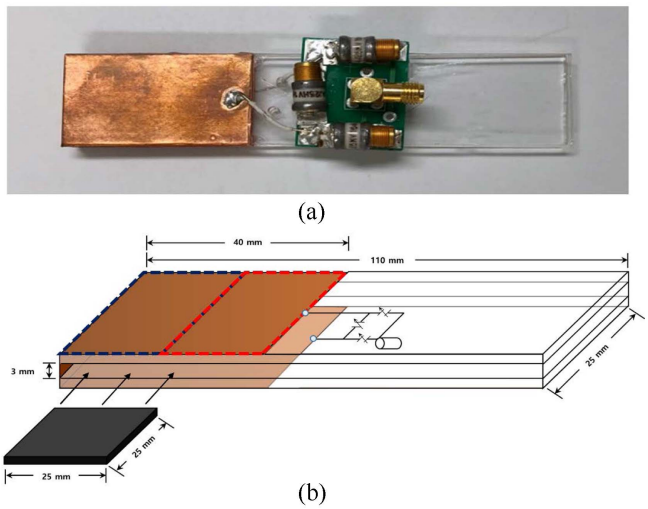

Fig. 4. (Color online) First version of planar RF coil for ^{1}H (a) picture of implemented ^{1}H planar RF coil (b) dimension of ^{1}H planar RF coil and sample.

The planar coils for ^{1}H fabricated under such principles were tuned and matched by fabricating additional circuits composed of variable capacitors on the conductor strips. This coil was tuned to 297.2 MHz, the resonance frequency of ^{1}H at 7T, and matched to operate in a 50 Ω device. In addition, as with the loop coil, the coil performance was evaluated with the reflection coefficient and Q-factor for the coil.

This coil forms a generally uniform B_1 field distribution in the area indicated by the dashed blue line in Fig. 4(b). However, the B_1 field decreases in areas closer to the strip edge, and increases in areas connected to the matching circuit, resulting in an uneven field distribution [12]. In Fig. 9(b), the dashed red line indicates an area in which the field distribution is uneven, and it is difficult to obtain uniform images in this area. Therefore, a new type of planar coil was devised to eliminate areas where the field distribution is uneven from existing planar coils.

2.3. Second Design of Planar Radio-Frequency Coils for ^{1}H and ^{7}Li

The cut coil (corner-cut planar RF coil) for ^{1}H proposed in Fig. 5 is a form of the existing planar coil from which the strip edge in which the B_1 field decreases was cut off. The conductor strip size on each acrylic plate was set at 50 mm × 25 mm, and about 10 mm of the strip edge was cut off in a triangular shape. Because this design makes the field distribution more uniform and increases the usable conductor area, improved of the overall coil performance can be expected. In the coil, a circuit consisting of two 0.6-pF capacitors and a variable capacitor was fabricated in addition to the conductor strip and was also tuned and matched. The frequency was tuned to 297.2 MHz, a resonance frequency of ^{1}H in 7T, and impedance matching was performed to operate in a 50 Ω device. The reflection coefficient was measured through a network analyzer, and the Q-factor was calculated.

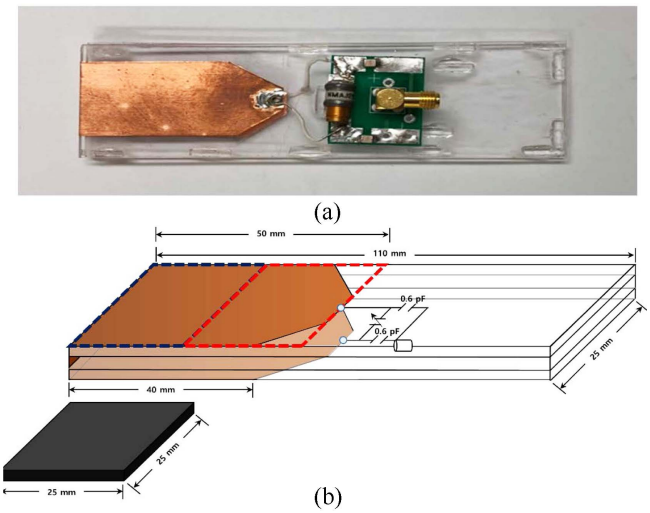

Fig. 5. (Color online) Second version of planar RF coil for ^{1}H (a) image of implemented ^{1}H corner-cut planar RF coil and (b) dimension of ^{1}H corner-cut planar RF coil and sample.

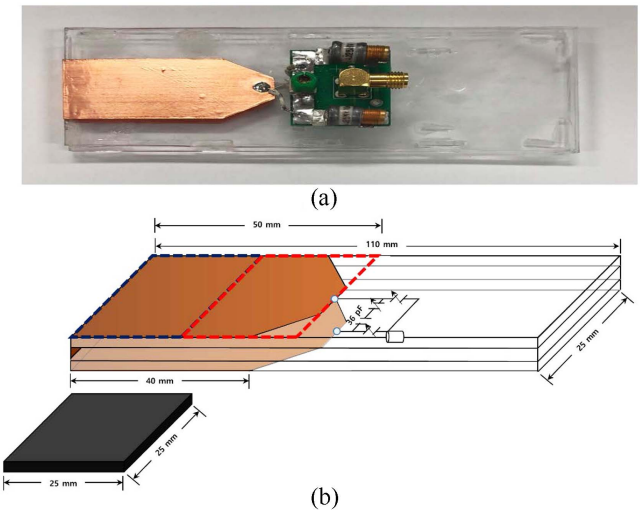

Fig. 6. (Color online) Second version of planar RF coil for ^{7}Li (a) image of implemented ^{7}Li corner-cut planar RF coil and (b) dimension of ^{7}Li corner-cut planar RF coil and sample.

The proposed cut coil for ^{7}Li in Fig. 6 has the same structure as the cut coil for ^{1}H, and the size of the conductor strip on each acrylic plate is 50 mm × 25 mm, and about 10 mm of the strip edge was cut off in a triangular shape. In the coil, a circuit consisting of a 36-pF capacitor and a variable capacitor was fabricated in addition to the conductor strip and was also tuned and matched. The frequency was tuned to 115.0 MHz, which is the resonance frequency of ^{7}Li at 7T, and impedance matching was performed to operate in a 50 Ω device. In addition, the coil performance was evaluated with the reflection coefficient and Q-factor for the coil.

2.4. System Environments, Parameters, and Materials

All experiments were conducted on a 7T whole-body MR system (Magnetom 7T, Siemens Healthcare, Erlangen, Germany). A water (H_2O) phantom was fabricated to compare the images and spectra of individual coils. For the phantom, the battery shape was reproduced by sealing the sample in a 25-mm × 30-mm × 2-mm square pouch made of polyethylene.

Loop, planar, and cut coils for ^{1}H were used to obtain images of the water phantom. The phantoms were placed in the front of the loop coils and between the acrylic plates of the planar and cut coils. A frequency shift by the

phantom occurred in the coils, and the experiments were conducted after tuning the coils to the corresponding frequencies. Images were acquired on the coronal plane of the phantoms, and the sequence parameters were repetition time (*TR*) = 400 ms, echo time (*TE*) = 5 ms, flip angle = 40°, field of view (*FOV*) = 56 mm × 56 mm, slice thickness = 1.5 mm, and matrix size = 256 × 256. The parameters were applied equally in all coil experiments. The sequence parameters for the ^{1}H spectrum data were *TR* = 10000 ms, *TE* = 0.2 ms, average = 10, which were obtained for the cases in which the bandwidth was set 3000 Hz or 6000 Hz.

To compare the effects of the shapes of the loop and planar coils in the acquired images, the signal strength profiles for individual coils were compared through MATLAB (MathWorks Inc., Natick, MA, USA). In the SNR of the images, the method of dividing the signal strength at the center of the phantom by the noise strength at the periphery was used based on the criteria defined by the National Electrical Manufacturers Association [14]. In addition, the ^{1}H and ^{7}Li spectra were obtained for the electrolyte phantoms with cut coils for ^{1}H and ^{7}Li. In this experiment, the phantoms were in the form of 1 mol of propylene carbonate-fluoroethylene carbonate electrolyte containing other materials, comprising three types, including those in which the lithium metal is attached to a copper plate and those in which the lithium metal is attached to the substrate. The phantom was placed between the acrylic plates of the cut coil, and because the frequency shift due to the phantom loading, each coil was re-tuned to the designated frequency. Images were acquired for the coronal plane of the phantom. The sequence parameters for ^{1}H images were *TR* = 400 ms, *TE* = 5 ms, flip angle = 45°, *FOV* = 56 mm × 56 mm, slice thickness = 5 mm, and matrix size = 256 × 256. These parameters were applied identically to the phantoms. The sequence parameters of the spectral data for ^{1}H were *TR* = 10000 ms, *TE* = 0.2 ms, average = 10, and the bandwidth was 3000 Hz or 6000 Hz. The sequence parameters of the ^{7}Li spectral data were *TR* = 3000 ms, *TE* = 0.2 ms, and average = 10, and the bandwidth was 3000 Hz or 6000 Hz.

3. Results and Analysis

3.1. Results of Coil Performances Comparison

Figure 7 presents the measurement results of the coil performance taken by measuring the reflection coefficient and Q-factor of the ^{1}H and ^{7}Li coils in the unloaded condition. Figure 7(a) is the measurement results of the reflection coefficient of the ^{1}H loop coil, and the reflection coefficient was measured as -30.93 dB for 297.2 MHz, the resonance frequency of ^{1}H in the 7T MR system. The coil Q-factor was calculated by obtaining the difference between the points at which the reflection coefficient decreased by 3 dB from the maximum value of the reflection coefficient spectrum. The 3-dB coil bandwidth was measured as 4.52 MHz, and the coil Q-factor was calculated as 65.75 in the unloaded condition. When the water phantom was placed in front of the coil, little change occurred in the Q-factor due to phantom loading. Figure 7(b) depicts the measurement results of the reflection coefficient of the loop coil for ^{7}Li. The reflection coefficient of the coil was measured as -29.86 dB for 115 MHz, the resonance frequency of ^{7}Li in a 7T MR system. The

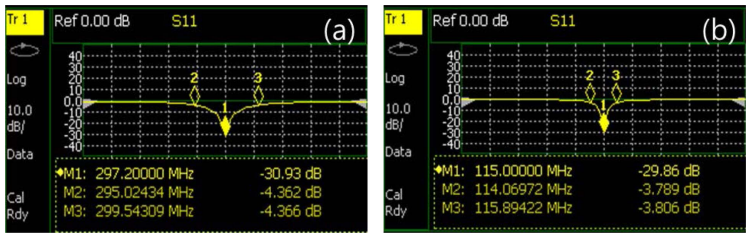

Fig. 7. (Color online) S_{11} of loop coil measured by network analyzer. (a) S_{11} of ^{1}H loop coil and (b) S_{11} of ^{7}Li loop coil.

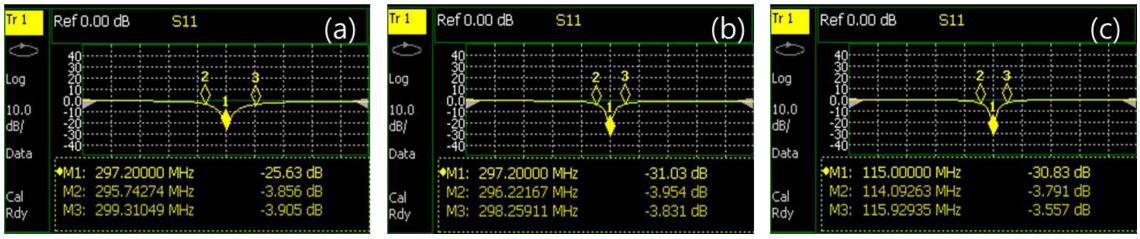

Fig. 8. (Color online) S_{11} of planar RF coil measured by network analyzer (a) S_{11} of ^{1}H planar RF coil, (b) S_{11} of ^{1}H cut coil, and (c) S_{11} of ^{7}Li cut RF coil.

Table 1. Coil performance comparison.

	Loop coil		Planar coil	Cut coil	
Nucleus	^{1}H	^{7}Li	^{1}H	^{1}H	^{7}Li
Resonance frequency (MHz)	297.2	115	297.2	297.2	115
Reflection coefficient (dB)	-30.93	-29.86	-25.63	-31.03	-30.83
Quality factor	65.75	63.19	82.25	145.69	62.84

3-dB coil bandwidth was measured as 1.82 MHz. The Q-factor was calculated as 63.19 in the unloaded condition.

Figure 8(a) presents measurement results of the reflection coefficient of the ^{1}H planar coils. The reflection coefficient of the coil was measured as -25.63 dB at 297.2 MHz. When the 3-dB bandwidth was 3.57 MHz, the coil Q-factor was calculated as 82.25 in the unloaded condition, and little influence of the load was found.

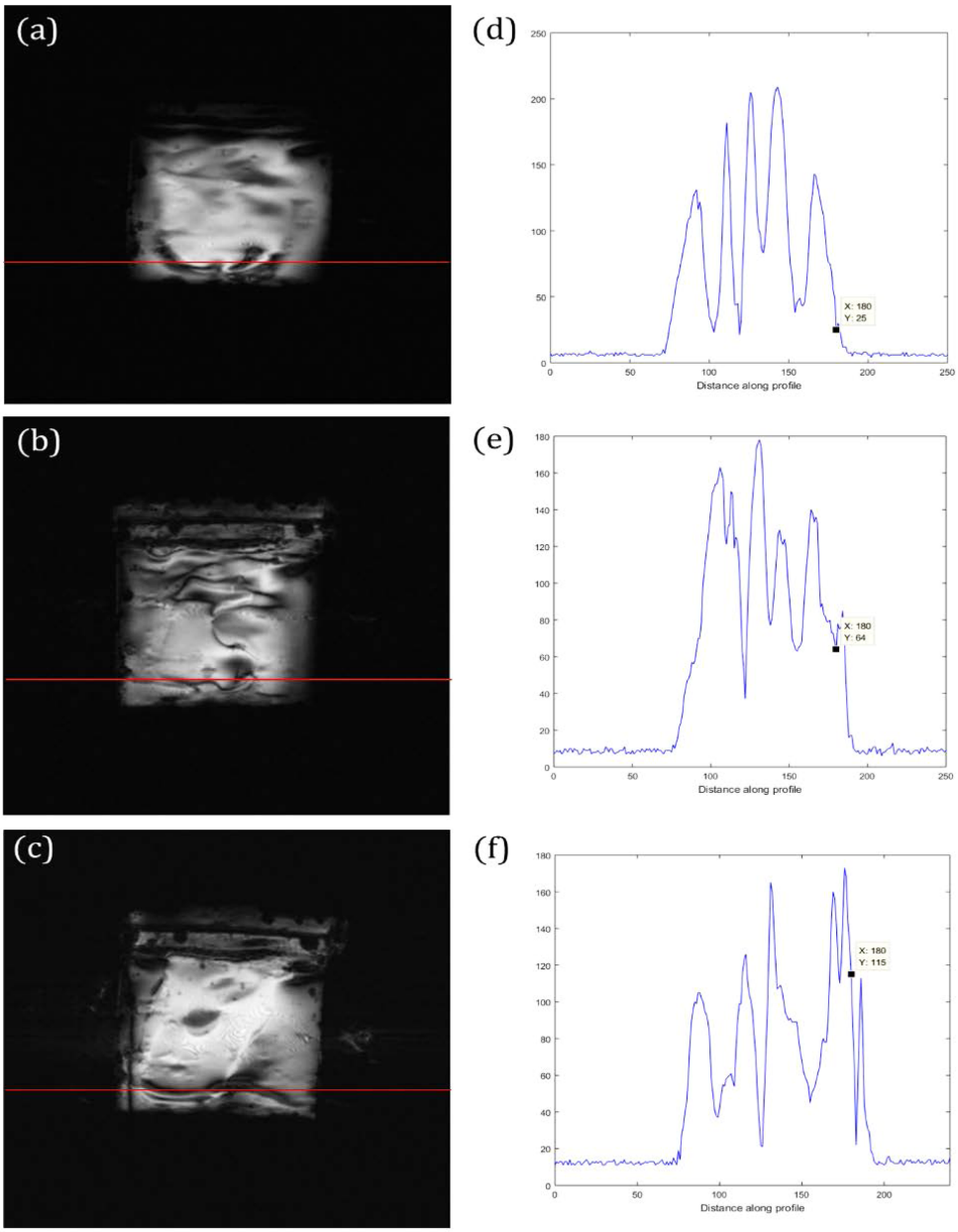

Fig. 9. (Color online) Phantom imaging and cut-profile with ^{1}H loop coil (a, d), ^{1}H planar coil (b, e), and ^{1}H cut coil (c, f). Profiles in the right column (d, e, f) present the signal strength of the red lines of the images in the left column.

Figure 8(b) displays the measurement results of the reflection coefficient of cut coils for ^{1}H. The reflection coefficient of the coils was measured as -31.03 dB, and the coil Q-factor was calculated as 145.69 in the unloaded condition when the 3-dB bandwidth was 2.04 MHz. Little influence of the load was observed. Figure 8(c) illustrates the reflection coefficient of the cut coils for ^{7}Li, which was measured as -30.83 dB at 297.2 MHz. The 3-dB coil bandwidth was measured as 1.84 MHz, and the Q-factor was calculated as 62.84.

Table 1 lists the results of comparing the electrical characteristics of the loop coils for ^{1}H and ^{7}Li, planar coils for ^{1}H, and cut coils for ^{1}H and ^{7}Li. For all coils, the reflection coefficients were at least -20 dB, indicating high transmission efficiency. Among the Q-factors for ^{1}H coils, those for cut coils exhibited the highest value at 145.69, followed by planar and loop coils in order of precedence, and the Q-factor values demonstrated large differences according to the coil shapes. Among the Q-factors for ^{7}Li coils, the Q-factor for loop coils exhibited a higher value than that for cut coils, but no significant difference exists between the two values.

3.2. ^{1}H Imaging and Signal-to-Noise Ratio

The ^{1}H images of the water phantom were acquired with loop, planar, and cut coils for ^{1}H, and the results were compared. The images in Fig. 9(a-c) present the coronal imaging of the phantom obtained with loop, planar, and cut coils for ^{1}H. The uneven area in the image results from the reflection of the structural features of the phantom, which is thin and has an uneven surface, and is also due to the artifacts from air bubbles existing inside the phantom. In each image, a signal intensity profile horizontally passing through the image was extracted to identify the effects of the coil shapes.

Figure 9(d-f) presents the signal strength profiles of the solid red lines in the images acquired with individual coils on the left. At the same position on the phantom

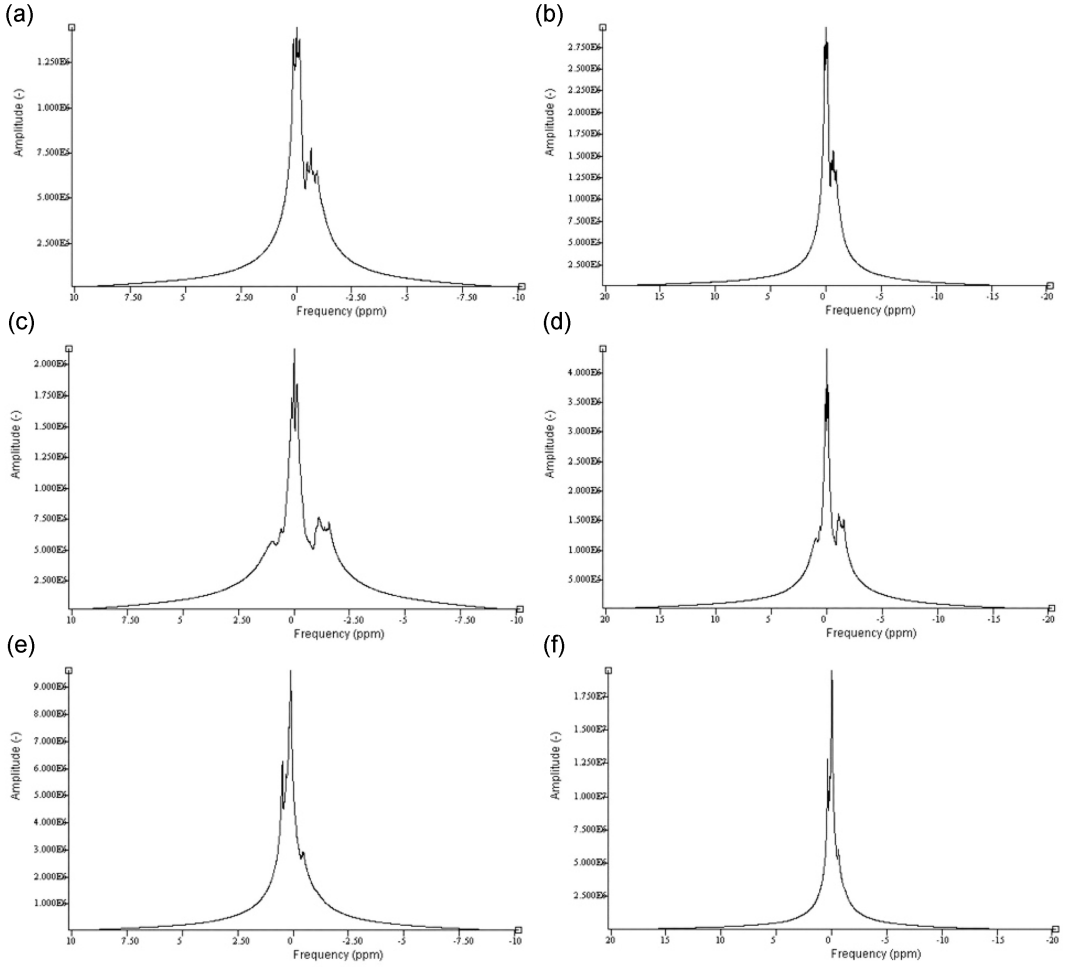

Fig. 10. The ^{1}H spectrum with loop coil (a, b), planar coil (c, d), and cut coil (e, f). Left column used 3000 Hz bandwidth; right column used 6000 Hz bandwidth.

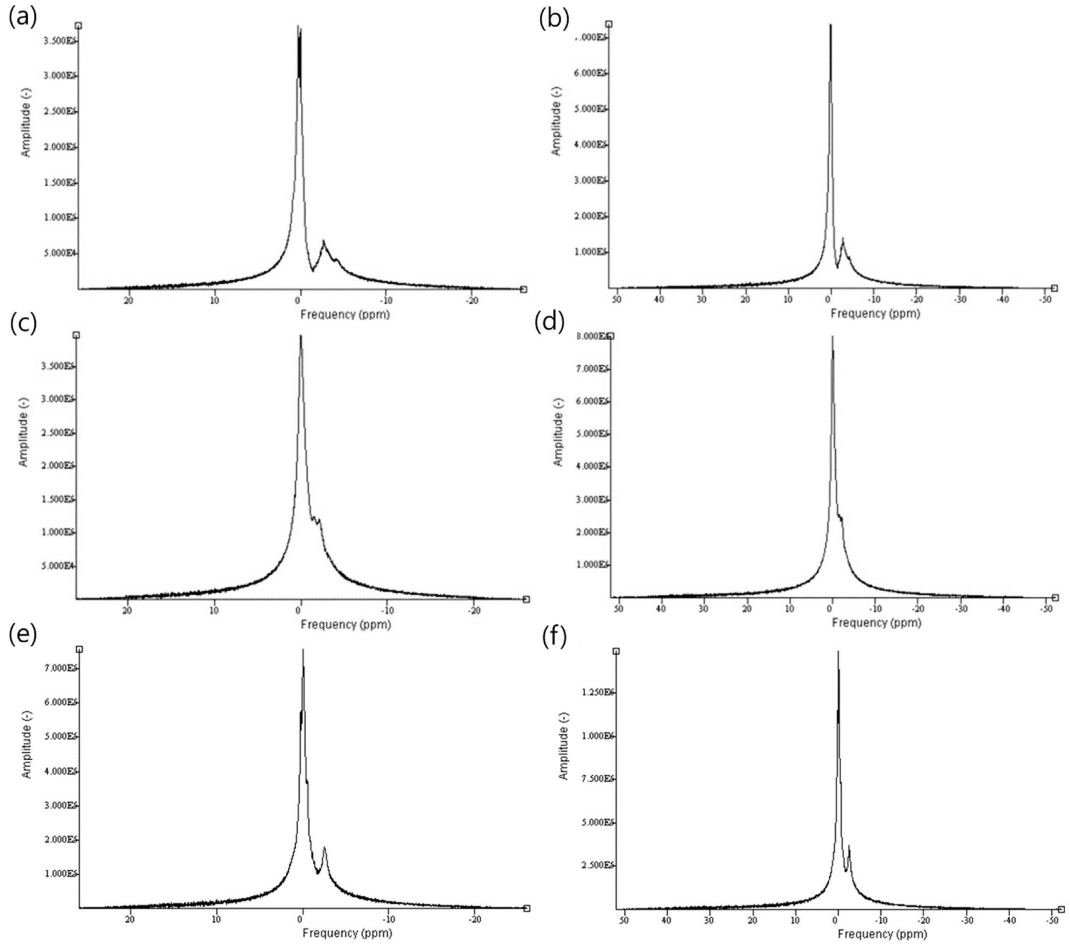

Fig. 11. The ^{7}Li spectrum of the phantom. Pouch contains a copper plate with soldered Li metal (a, b), an isolated copper plate on a fiber-glass plate without Li metal (c, d), and an isolated copper plate on a fiber-glass plate with Li metal (e, f). Left column used 3000 Hz bandwidth; right column used 6000 Hz bandwidth.

edge, the loop coil signals had lower values than those of the planar coil and cut coil signals.

In addition, the SNRs were measured and compared using the image in Fig. 10. The SNRs were calculated as 128.067 for loop coils, 83.382 for planar coils, and 137.735 for cut coils. Therefore, the highest value was for cut coils. When the SNR of the cut coils was set as the standard, the SNR of planar coils was 61 % of that of cut coils, indicating a value lower than that of the cut and loop coils. The SNR of loop coils was close to that of the cut coils (93 % of cut coils).

3.3. Spectrum of ^{1}H and ^{7}Li

Figure 10 illustrates the spectra obtained with individual ^{1}H coils for the electrolyte phantom. The spectra were obtained for the cases in which the bandwidth was 3000 Hz or 6000 Hz. When the chemical shift of water was set to 0 ppm, the signals for water were detected in the spectra for all coils.

Figure 11 displays the spectrum using a cutting coil for ^{7}Li for the electrolyte phantom, including the substrate. The images in Fig. 11(a, b) are the experimental results for an electrolyte pouch phantom with the lithium metal attached to the copper plate, and Fig. 11(c, d) indicates the experimental results for an electrolyte phantom with nine copper plates on the substrate. Finally, Fig. 11(e, f) presents the experimental results for an electrolyte phantom with the lithium metal attached to some part of the substrate. The bandwidth was obtained for the cases in which the bandwidth was 3000 Hz (left column) and 6000 Hz (right column).

4. Conclusion

The reflection coefficients for all surface coils typically exhibited high values, and the coils operated normally at their corresponding resonance frequencies. The coil Q-factor demonstrated the lowest value in loop coils and the

highest value in cut coils in the unloaded condition. According to the coil shapes, this outcome results from the differences in the resistance and inductance values because the Q-factor is inversely proportional to the resistance is proportional to the inductance [15]. In addition, the reason the coil Q-factor did not reveal any large change when a load was applied could be because the effect on the coils was small due to the size of the phantom used and the small number of samples. The ^{7}Li coil, which operate in lower frequency bands than ^{1}H, did not exhibit a large difference in the Q-factor values by shape compared to the coils for ^{1}H.

The ^{1}H images of the coil acquired from the coronal surface of the water phantom revealed the structural limitations of the loop coils. Because the loop coils and phantom are structurally inconsistent, low signals were detected, especially at the phantom edge. Thus, in the experiments to acquire battery cell images, using planar coils is more suitable than using loop coils.

The SNRs for individual images were expected to be affected by the coil Q-. As a result of the measurement, the SNR exhibited the highest value in the cut coils, which is related to the fact that the Q-factor of the cut coils had much higher values compared to those of the loop or planar coils [16]. However, the SNR for the images acquired with the loop coils was higher than that of the planar coils with high Q-factors.

Primarily, three factors affected the results. The first factor is that the distance from the loop coil to the phantom is shorter than the distance from the planar coil to the phantom because of the structure. The difference between the two coils might have affected the SNRs because a shorter distance between the coil and phantom, results in a higher SNR.

Second, the change in the phantom might have affected the results. Because the phantom used in the experiment was sealed with a polyethylene pouch, the appearance changes easily, even at low pressure. Therefore, different results for images might have been acquired because the appearance of the phantom changed when the images were acquired with loop and planar coils.

Third, the results might have been affected by high Q-factors. Because the designed coils have high Q-factors, when a frequency shift occurs, the transmission efficiency decreases significantly. These factors might have affected the reduction in the SNRs.

When obtained for the coronal surface of each electrolyte phantom, the structural characteristics of the phantom could be easily observed with the naked eye in the ^{1}H and ^{7}Li images. However, because the cut coils for ^{1}H and ^{7}Li could not be simultaneously used when acquiring images

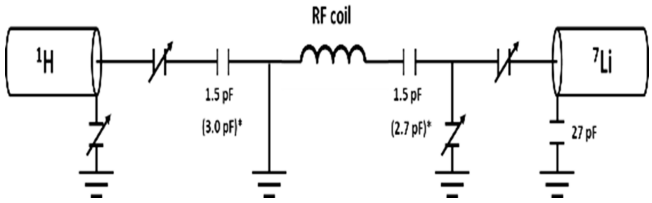

Fig. 12. Circuit diagram of the feeding board for a dual-tuned RF coil.

because of the structures, positional differences occurred between the ^{1}H and ^{7}Li images, causing difficulties in the comparison. A feeding board was designed for dual-tuned coils that can be used in 7T MRI to solve this problem (Fig. 12). Images can be acquired at the same location using this coil, even if the nuclide is changed because this coil can operate in two desired frequency bands [16-20]. The spectra extracted from the electrolyte phantom demonstrated similar results for all phantoms. In particular, it was confirmed that ^{7}Li signals can be obtained from an MR system by confirming that a lithium ion component is detected at 2 ppm of the ^{7}Li spectrum.

Acknowledgements

This research was supported by a grant of the Korea Health Technology R&D Project through the Korea Health Industry Development Institute, funded by the Ministry of Health & Welfare, Republic of Korea (grant number: HI14C1135).

This research was supported by the Gachon University research fund of 2015 (GCU-2015-0062) and 2016 (GCU-2016-0054).

References

[1] M Armand and J. M. Tarascon, Nature **414**, 359 (2001).
[2] D. Deng, M. G. Kim, J. Y. Lee, and J. Cho, Energy Environ. Sci. **2**, 818 (2009).
[3] D. Deng, Energy Sci. & Engin. **3**, 385 (2015).
[4] N. M. Trease, L. Zhou, H. J. Chang, B. Y. Zhu, and C. P. Grey, Solid State Nucl. Magn. Reson. **43**, 62 (2012).
[5] K. Shimoda, M. Murakami, D. Takamatsu, H. Arai, Y. Uchinoto, and Z. Ogumi, Electrochimica Acta **108**, 343 (2013).
[6] B. Comes, P. F. da Silva, C. M. S. Lobo, M. S. da Silva, and L. A. Colnago, Analytica Chimica Acta **983**, 91 (2017).
[7] A. J. Ilott, M. Mohammadi, C. M. Schauerman, M. J. Ganter, and A. Jerschow, Nature Commun. **9**, 1776 (2018).
[8] A. J. Ilot, M. Mohammadi, H. J. Chang, C. P. Grey, and A. Jerschow, Proc. National Academy Sci. **113**, 10779

(2016).
[9] S. Chandrashekar, N. M. Trease, H. J. Chang, L. S. Du, C. P. Grey, and A. Jerschow, Nature Mater. **11**, 311 (2012).
[10] N. M. Britton, P. M. Bayley, P. C. Howlett, A. J. Devenport, and F. Forsyth, J. Phys. Chem. Lett. **4**, 3019 (2013).
[11] J. A. Tang, S. Dugar, G. Zhong, N. S. Dalal, J. P. Zheng, T. Yang, and R. Fu, Sci. Rep. **3**, 2596 (2013).
[12] S. Li, Q. X. Yang, and M. B. Smith, Magn. Reson. Imaging **12**, 1079 (1994).
[13] M. D. Meadowcroft, S. Zhang, W. Liu, B. S. Park, J. R. Connor, C. M. Collins, M. B. Smith, and Q. X. Yang, Magn. Reson. Med. **57**, 835 (2007).
[14] National Electrical Manufacturers Association (NEMA), Determination of signal to noise ratio (SNR) in diagnostic magnetic resonance imaging. NEMA Standards Publication. Rosslyn, VA (2008).
[15] C. Massin, G. Boero, F. Vincent, J. Abenhaim, P. A. Basse, and R. S. Popovic, Sensors Actuators A: Physical **97**, 280 (2002).
[16] H. Lim, K. Thind, F. M. Martinez-Santiesteban, and T. J. Scholl, J. Magn. Reson. Imaging **40**, 1082 (2014).
[17] S. Ha, M. J. Hamamura, O. Nalcioglu, and L. T. Muftuler, Physics Med. Biol. **55**, 2589 (2010).
[18] C. H. Moon, J. H. Kim, T. Zhao, and K. T. Bae, J. Magn. Reson. Imaging **38**, 1063 (2013).
[19] M. Alecci, S. Romanzetti, J. Kaffanke, A. Celik, H. P. Wegener, and N. J. Shah, J. Magn. Reson. **181**, 203 (2006).
[20] X. Yan, R. Xue, and X. Zhang, Quant. Imaging Med. Surg. **4**, 225 (2014).